Three-Phase Two-Level VSIs With Significant PWM Harmonics Dispersion and Improved Performance Using Generalized *N*-State Random Pulse Position SVPWM With Constant Sampling Frequency

Peiran Zhang, Shanming Wang, *Senior Member, IEEE*, and Yituo Li

***Abstract*—Constant sampling frequency, excellent pulsewidth modulation (PWM) harmonics dispersion performance, and avoidance or reduction of extra switching counts (ESCs) are three important factors in evaluating the performance of different random PWM (RPWM) strategies in closed-loop control systems. However, existing strategies cannot achieve all these three important factors at the same time. Therefore, this article proposes generalized *N*-state random pulse position space vector pulsewidth modulation (GNSRPP-SVPWM) to achieve these three important factors at the same time. GNSRPP-SVPWM randomly selects one of the well-designed carrier patterns for each carrier period. Compared with random carrier frequency PWM whose sampling frequency varies with the carrier frequency, GNSRPP-SVPWM maintains constant sampling frequency, thereby achieving applicability in closed-loop control systems. Compared with fixed carrier frequency RPWM (FCF-RPWM) without ESCs, GNSRPP-SVPWM has much better PWM harmonics dispersion performance. Compared with the traditional FCF-RPWM with ESCs, GNSRPP-SVPWM has the same excellent PWM harmonic dispersion performance while significantly reducing single-phase ESCs and completely avoiding simultaneous two- or three-phase switching operations, thereby improving the inverter performance. By mathematical analysis, the PWM harmonic dispersion principle and avoidance or reduction of ESCs for different GNSRPP-SVPWM strategies are discussed in detail. Both simulations and experiments verify the effectiveness of GNSRPP-SVPWM at last.**

***Index Terms*—Constant sampling frequency, extra switching counts (ESCs), pulsewidth modulation (PWM) harmonics dispersion, random carrier pattern, space vector pulsewidth modulation (SVPWM).**

I. Introduction

AS THE energy issue becomes more relevant to the daily life and environmental protection, voltage source inverter (VSI) applications and technology development are one of the important research topics because VSIs can provide variable voltage and frequency by pulsewidth modulation (PWM) technology to adjust the speed of motor drives and save electrical power consumption [1], [2].

Conventional space vector PWM (SVPWM) has inherent side effects such as high-frequency harmonics, electromagnetic interference (EMI), and noise vibration and harshness (NVH). Among these side effects, the output high-frequency voltage harmonics of VSIs are responsible for high-frequency vibrations and noises of motor drives, since the range of human hearing usually overlaps with the switching frequency [3], [4].

RLC filter [5] and parallel interleaved inverters [6] can effectively suppress high-frequency PWM harmonics, but they increase the cost and complexity of the control system.

Random PWM (RPWM) strategy is the effective and costless method to solve aforementioned problems [7]. From the angle of control parameters, RPWM strategies can be classified into random carrier frequency PWM (RCF-PWM) and fixed carrier frequency RPWM (FCF-RPWM). Feasibility in closed-loop control systems, PWM harmonics dispersion performance and extra switching counts (ESCs) are three important factors in evaluating the performance of different RPWM strategies.

Generally speaking, RCF-PWM has better PWM harmonic dispersion performance than FCF-RPWM [8], [9]. In recent years, in order to achieve better PWM harmonics dispersion performance, optimizing the probability density distribution function is the further development of RCF-PWM strategies [10], [11], [12]. Besides, periodic carrier frequency PWM(PCF-PWM) is also evolving to find the optimal periodic profiles [13], further reduce the maximum spectral peak [14], and suppress NVH of motor drives [15], [16].

However, in most of the practical applications, the control algorithm is synchronized with the switching; therefore, the variable carrier frequency will deteriorate the performance of closed-loop applications, which is one of the disadvantages of RCF-PWM and PCF-PWM strategies [17], [18], [19], [20], [21], [22]. The modulator forms only a part of a larger control scheme designed with a specific bandwidth, dependent on the sampling frequency [20]. The variation of the current sampling frequency caused by variable carrier frequency affects the bandwidth and

Manuscript received 12 February 2023; revised 5 June 2023, 31 July 2023, and 10 September 2023; accepted 23 October 2023. Date of publication 27 October 2023; date of current version 6 December 2023. Recommended for publication by Associate Editor I. Slama-Belkhodja. *(Corresponding author: Shanming Wang.)*

The authors are with the State Key Laboratory of Control and Simulation of Power System and Generation Equipment, Department of Electrical Engineering, Tsinghua University, Beijing 100084, China (e-mail: zpr23@mails.tsinghua.edu.cn; wangsm96@mails.tsinghua.edu.cn; liyituo@mail.tsinghua.edu.cn).

Color versions of one or more figures in this article are available at https://doi.org/10.1109/TPEL.2023.3328213.

Digital Object Identifier 10.1109/TPEL.2023.3328213

related controller design specifications, which are required not to be changed in a closed-loop digitally controlled system [19].

One of the most important factors in the development of RPWM techniques for closed-loop digitally controlled systems is maintaining a constant sampling frequency [19]. FCF-RPWM strategies maintain a constant sampling frequency and are suitable for a closed-loop digitally controlled system with feedback control. However, before introducing ESCs, the relatively poor PWM harmonic performance made FCF-RPWM not gain much popularity [11]. FCF-RPWM strategies without ESCs can be divided into random lead-lag PWM (RLL-PWM), random center displacement PWM (RCD-PWM), and random zero vector distribution PWM (RZD-PWM) [23]. Their PWM harmonics dispersion performance is poor when the modulation ratio is high because the short time durations of zero-voltage vectors limit the randomization range.

To improve the PWM harmonics dispersion performance, ESCs at the boundaries of the carrier periods are introduced. In [24], [25], [26], and [27], the FCF-RPWM strategy using a random number generator to randomly select inverted and noninverted triangular carrier patterns has been verified to significantly disperse the odd order PWM harmonics. However, simultaneous three-phase switching operations will occur at the boundaries of the carrier periods in three-phase VSIs. In fact, this strategy is a special case of N-state random pulse position SVPWM (NSRPP-SVPWM) proposed in [28] when $N = 2$. In contrast, one of the strategies proposed in this article, G2SRPP-SVPWM, can also significantly disperse the odd-order PWM harmonics, but does not lead to any ESC.

Zhang et al. [28] proposed NSRPP-SVPWM to further explore the combination of more carrier patterns. NSRPP-SVPWM has been verified to significantly disperse all PWM harmonics except those located nearby the Nth carrier frequency and its multiples. However, for NSRPP-SVPWM, ESCs may occur at the boundaries of the carrier periods, which will bring some disadvantages. Switching losses will increase, and inverter efficiency will decrease. To make the situation worse, simultaneous two- or three-phase switching operations are prohibited in practical applications [29], [30], [31], [32]. In general, switching two or more phases at the same time is problematic in the sense of noise generation and nuisance trips, and it will produce interference and strongly influence the performance stability of inverters. And an instantaneous line-to-line voltage reversal results in significant overvoltages at the motor terminals (in particular, in long cable applications, where cable capacitance is large) [30]. Based on aforementioned problems, the simultaneous switching of at least two phases at a time must be avoided in practical applications.

Generalized NSRPP-SVPWM (GNSRPP-SVPWM) proposed in this article aims to further overcome the shortcomings of NSRPP-SVPWM leading to ESCs. Therefore, the proposed GNSRPP-SVPWM can achieve constant sampling frequency, excellent PWM harmonics dispersion performance, and avoidance or reduction of ESCs at the same time. The proposed GNSRPP-SVPWM is implemented by randomly selecting one of the well-designed fundamental carrier patterns for each carrier period. NSRPP-SVPWM represents a specific instance of GNSRPP-SVPWM, which is actually the worst case for the inverter performance.

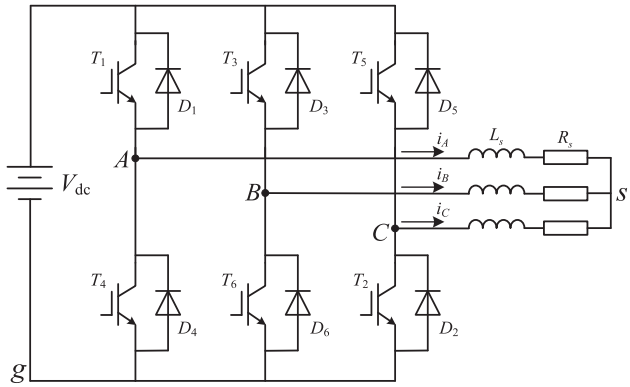

Fig. 1. Circuit topology of three-phase two-level VSI.

The rest of this article is organized as follows. Section II introduces the working process of the proposed GNSRPP-SVPWM, and explains the principle of PWM harmonics dispersion. In Section III, the occurrence probabilities of three types of ESC (single-phase ESC, simultaneous two-phase switching operation, and simultaneous three-phase switching operation) are calculated, and several strategies are recommended. Section IV analyzes the switching power losses of the proposed GNSRPP-SVPWM. In Section V, simulations conducted in MATLAB/Simulink are observed and analyzed in detail. In Section VI, experiments conducted on an IPMSM sensorless drive system verify the effectiveness of some recommended strategies. Comparison with other RPWM strategies is also provided in both simulations and experiments. Finally, Section VII concludes this article.

II. Introduction and PWM Harmonics Analysis of the Proposed GNSRPP-SVPWM

As shown in Fig. 1, the traditional three-phase two-level VSI is the research object of this article. In the differential-mode (DM) domain, the phase voltage V_{As} is defined by the three-phase leg voltages V_{Ag}, V_{Bg}, and V_{Cg} as follows:

$$V_{As} = \frac{1}{3}\left(2V_{Ag} - V_{Bg} - V_{Cg}\right). \tag{1}$$

Obviously, in the DM domain, the phase voltage determines the variation of the phase current.

In the common-mode (CM) domain, the CM voltage (CMV) is defined as follows:

$$\mathrm{CMV} = \frac{1}{3}\left(V_{Ag} + V_{Bg} + V_{Cg}\right). \tag{2}$$

A. Reference Wave

Define the normalized three-phase voltages as VN_{A}, VN_{B}, and VN_{C}, they meet

$$VN_A(t) = \frac{2}{\sqrt{3}} a \cdot \cos\left(\omega_0 t\right)$$

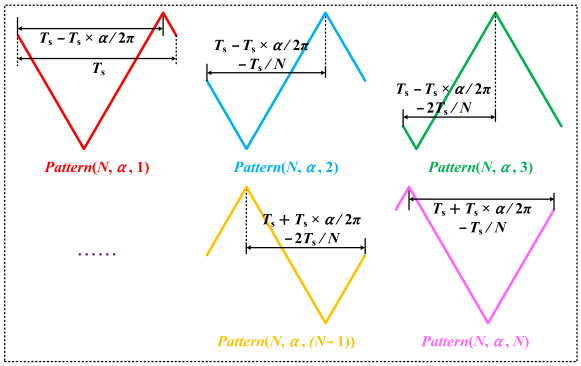

Fig. 2. Fundamental carrier patterns of GNSRPP-SVPWM(N, α).

$$VN_B(t) = \frac{2}{\sqrt{3}}a \cdot \cos\left(\omega_0 t - \frac{2}{3}\pi\right)$$
$$VN_C(t) = \frac{2}{\sqrt{3}}a \cdot \cos\left(\omega_0 t + \frac{2}{3}\pi\right) \quad (3)$$

where ω_0 is the angular fundamental frequency, and the modulation ratio a is defined as:

$$a = \frac{\sqrt{3}}{V_{\rm dc}}|V_{As\_fun}| \quad (4)$$

where $|V_{As\_fun}|$ is the amplitude of the fundamental component of the phase voltage, $V_{\rm dc}$ is the dc-link voltage, and $0 \le a \le 1$.

In the following description, $VN_{\rm mid}$ is the medium value of the normalized three-phase voltages. When the time durations of the two zero-voltage vectors are equal, the injected zero-sequence voltage is calculated to be "$0.5 \times VN_{\rm mid}(t)$." Therefore, the three-phase reference waves are expressed as

$$VR_A(t) = \frac{2}{\sqrt{3}}a \cdot \cos(\omega_0 t) + \frac{1}{2} \cdot VN_{\rm mid}(t)$$
$$VR_B(t) = \frac{2}{\sqrt{3}}a \cdot \cos\left(\omega_0 t - \frac{2}{3}\pi\right) + \frac{1}{2} \cdot VN_{\rm mid}(t)$$
$$VR_C(t) = \frac{2}{\sqrt{3}}a \cdot \cos\left(\omega_0 t + \frac{2}{3}\pi\right) + \frac{1}{2} \cdot VN_{\rm mid}(t). \quad (5)$$

B. Working Process

For the convenience of description, GNSRPP-SVPWM with N fundamental carrier patterns and the initial carrier phase-shift angle α is named GNSRPP-SVPWM(N, α) in this article.

For GNSRPP-SVPWM(N, α), Fig. 2 shows the N fundamental carrier patterns with the initial carrier phase-shift angle α, and there is a carrier phase-shift angle of $2\pi/N$ or its multiple between each pair of them. "*Pattern*(N, α, i)" is the ith fundamental carrier pattern. And the initial carrier phase-shift angle α satisfies that "$0 \le \alpha < \frac{2\pi}{N}$." Then, the carrier phase-shift angles of the N fundamental carrier patterns are α, $(\alpha + \frac{2\pi}{N})$, $(\alpha + 2 \times \frac{2\pi}{N})$, …, $(\alpha + (N-2) \times \frac{2\pi}{N})$ and $(\alpha + (N-1) \times \frac{2\pi}{N})$, respectively.

NSRPP-SVPWM represents the specific instance of GNSRPP-SVPWM (N, α) when $\alpha = 0$. Conventional SVPWM represents the specific instance when $N = 1$ and $\alpha = 0$.

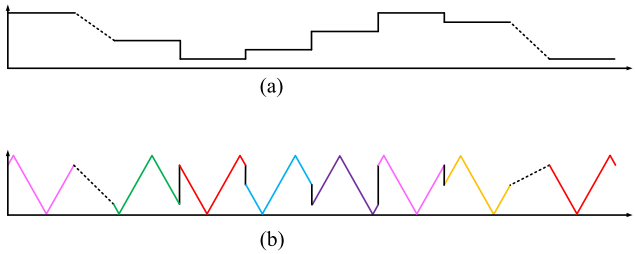

Fig. 3. Working process. (a) Random number. (b) Carrier.

As shown in Fig. 3(a) and (b), in the working process, a random number generator is used to randomly select one of the N fundamental carrier patterns with equal probability for each carrier period.

C. PWM Harmonics Dispersion Principle

The common method of PWM harmonic analysis is 2-D Fourier analysis. In 2-D Fourier analysis, the two dimensions map time t into the period of the carrier ($x = 2\pi f_c t = \omega_c t$) and the period of the modulating function ($y = 2\pi f_o t = \omega_o t$) [33]. Time-varying phase leg voltage can be expressed in terms of its PWM harmonic components as follows:

$$V_{Ag}(t) = \frac{V_{dc}}{2} + \sum_{n=1}^{\infty}\left[A_{0n}\cos(n\omega_0 t) + B_{0n}\sin(n\omega_0 t)\right] + \sum_{m=1}^{\infty}\sum_{n=-\infty}^{\infty}\left[A_{mn}\cos(m\omega_c t + n\omega_0 t) + B_{mn}\sin(m\omega_c t + n\omega_0 t)\right] \quad (6)$$

where m is the carrier index variable, n is the baseband index variable, A_{mn} and B_{mn} are the amplitudes of the PWM harmonic components, and ω_c is the angular carrier frequency.

The phase voltage, V_{As} is expressed as

$$V_{As} = \frac{1}{3}(2V_{Ag} - V_{Bg} - V_{Cg}) = \frac{2}{3}\sum_{n=1}^{\infty}\left(\left(1 - \cos\left(\frac{2}{3}n\pi\right)\right) \cdot \begin{bmatrix} A_{0n}\cos(n\omega_0 t) \\ +B_{0n}\sin(n\omega_0 t)\end{bmatrix}\right) + \frac{2}{3}\sum_{m=1}^{\infty}\sum_{n=-\infty}^{\infty}\left(\left(1 - \cos\left(\frac{2}{3}n\pi\right)\right) \cdot \begin{bmatrix} A_{mn}\cos(m\omega_c t + n\omega_0 t) \\ +B_{mn}\sin(m\omega_c t + n\omega_0 t)\end{bmatrix}\right). \quad (7)$$

CMV is expressed as

$$\text{CMV} = \frac{1}{3}(V_{Ag} + V_{Bg} + V_{Cg}) = \frac{V_{dc}}{2} + \frac{1}{3}\sum_{n=1}^{\infty}\left(\left(1 + 2\cos\left(\frac{2}{3}n\pi\right)\right) \cdot \begin{bmatrix} A_{0n}\cos(n\omega_0 t) \\ +B_{0n}\sin(n\omega_0 t)\end{bmatrix}\right)$$

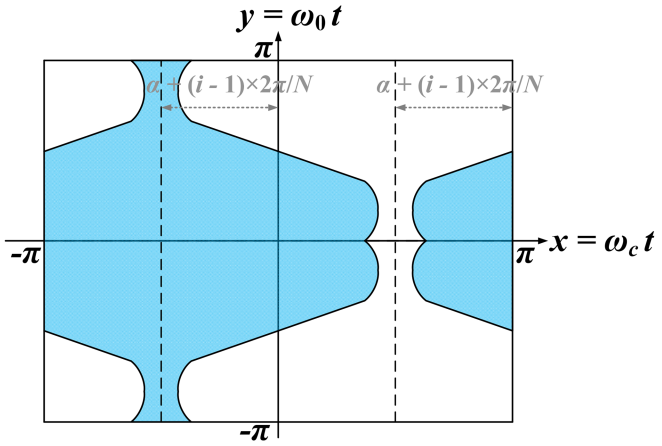

Fig. 4. Unit cell of the carrier pattern *pattern* (N, α, i) for double Fourier integral.

$$+\frac{1}{3}\sum_{m=1}^{\infty}\sum_{n=-\infty}^{\infty}\left(\left(1+2\cos\left(\frac{2}{3}n\pi\right)\right)\cdot\begin{bmatrix}A_{mn}\cos\left(m\omega_c t+n\omega_0 t\right)\\+B_{mn}\sin\left(m\omega_c t+n\omega_0 t\right)\end{bmatrix}\right). \tag{8}$$

For the proposed GNSRPP-SVPWM, the unit cell of the carrier pattern *Pattern*(N, α, i) for the double Fourier integral is shown in Fig. 4. The PWM harmonic component with naturally sampled modulation is given as

$$\begin{aligned}&A_{mn}+jB_{mn}\\&=\frac{1}{2\pi^2}\int_{-\pi}^{\pi}\int_{x_r}^{x_f}V_{dc}e^{j\left(m\left(x+\left(\alpha+(i-1)\times\frac{2\pi}{N}\right)\right)+ny\right)}dxdy\\&=e^{jm\alpha}\cdot e^{j\cdot(i-1)\times\frac{2m\pi}{N}}\cdot\frac{1}{2\pi^2}\int_{-\pi}^{\pi}\int_{x_r}^{x_f}V_{dc}e^{j(mx+ny)}dxdy\\x_f&=\frac{\pi}{2}\left(1+\frac{2a}{\sqrt{3}}\cos\left(y\right)+\frac{1}{2}\cdot VN_{\text{mid}}\left(y\right)\right)\\x_r&=-\frac{\pi}{2}\left(1+\frac{2a}{\sqrt{3}}\cos\left(y\right)+\frac{1}{2}\cdot VN_{\text{mid}}\left(y\right)\right).\end{aligned} \tag{9}$$

There are two important multiplication factors in (9), i.e., "$e^{jm\alpha}$" and "$e^{j\cdot(i-1)\times\frac{2m\pi}{N}}$." For different fundamental carrier patterns, i.e., for different values of i, the initial carrier phase-shift angle α only exists in "$e^{jm\alpha}$" and it does not affect the amplitudes of PWM harmonic component coefficients. Although the initial carrier phase-shift angle α does not affect the PWM harmonics dispersion performance, a well-designed α plays an important role in avoiding or reducing ESCs, which will be discussed in detail in Section III.

The second multiplication factor "$e^{j\cdot(i-1)\times\frac{2m\pi}{N}}$" is important in explaining the principle of dominant PWM harmonics dispersion. According to [28], the harmonic coefficients of random schemes can be seen as the average of the 2-D Fourier integrals corresponding to different unit cells. Since the random generator randomly selects one of the N fundamental carrier patterns for each carrier period, harmonic dispersion coefficient (HDC) can be defined by complex vectors as

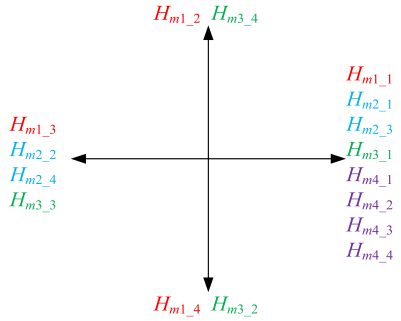

Fig. 5. Complex vector diagram of HDC for G4SRPP-SVPWM(4, α).

$$\text{HDC}=\left|\frac{1}{N}\cdot\sum_{i=1}^{N}e^{j\cdot(i-1)\times\frac{2m\pi}{N}}\right|=\begin{cases}0, m\neq Nk+N\\1, m=Nk+N\end{cases} \tag{10}$$

where $k=0, 1, 2, 3, \ldots$. When $m\neq(Nk+N)$, different complex vectors can cancel each other out due to the phase difference, so the corresponding HDC value is 0. Due to the same direction of different complex vectors when $m=(Nk+N)$, the corresponding HDC value is 1. Therefore, it can be deduced that the random selection from N fundamental carrier patterns will significantly disperse the ($Nk+1$)th, ($Nk+2$)th, …, ($Nk+N-2$)th and ($Nk+N-1$)th dominant PWM harmonics, while the ($Nk+N$)th dominant PWM harmonics remain unchanged.

For example, the complex vector diagram of G4SRPP-SVPWM(4, α) is shown in Fig. 5, where H_{mv_i} is the (i)th complex vector when $m=(4k+v)$, $k=0, 1, 2, 3, \ldots$, and $v=1, 2, 3, 4$. When $m=(4k+1)$, $(4k+2)$, and $(4k+3)$, the superposition of complex vectors with different phase differences significantly attenuates their HDC and the ($4k+1$)th, ($4k+2$)th, and ($4k+3$)th PWM harmonics. But when $m=(4k+4)$, the same complex vector direction keeps its HDC and the ($4k+4$)th PWM harmonics unchanged.

As a comparison, since conventional SVPWM represents the specific instance when $N=1$ and $\alpha=0$, its HDC is always 1. Dominant PWM harmonics will appear around the carrier frequency and its multiples when using conventional SVPWM.

III. Calculation for the Occurrence Probabilities of ESCs

A. Introduction of ESCs

ESCs include three types of switching operations, i.e., single-phase ESC, simultaneous two-phase switching operation, and simultaneous three-phase switching operation. Single-phase ESC is for any one of the three phases, regardless of the other two phases. Simultaneous two-phase switching operation means that the power devices of any two phases are switched at the same time, while the power devices of the other phase are not switched. Simultaneous three-phase switching operation means that the power devices of all three phases are switched at the same time.

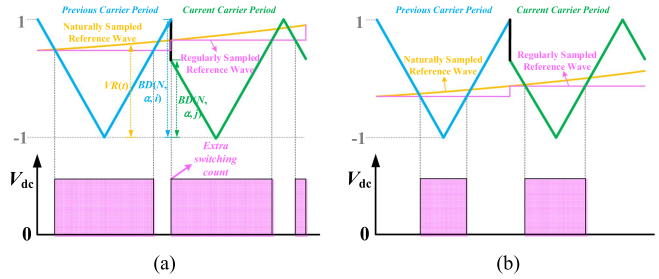

Fig. 6. Diagram of single-phase ESC between the previous carrier pattern *pattern*(*N*, α, *i*) and the current carrier pattern *pattern*(*N*, α, *j*). (a) When single-phase ESC occurs. (b) When single-phase ESC does not occur.

The diagram of the single-phase ESC is shown in Fig. 6, where the reference wave is intersected with symmetrical triangular carrier wave ranging from −1 to 1 to obtain the output phase leg voltage. From Fig. 6, it can be deduced that a single-phase ESC occurs only when the reference wave value is between the previous carrier pattern boundary and the current carrier pattern boundary.

To make the situation worse, when the two- or three-phase reference wave values are between the previous carrier pattern boundary and the current carrier pattern boundary, simultaneous two- or three-phase switching operations will occur. They are prohibited in practical application due to the electromagnetic noise, nuisance trips, and instantaneous line-to-line voltage reversals [29], [30], [31], [32].

B. Boundary Values of Fundamental Carrier Patterns

The design of the fundamental carrier patterns is important because their boundary values significantly affect the occurrence of ESCs. For GNSRPP-SVPWM(*N*, α), the boundary value of the fundamental carrier pattern *Pattern*(*N*, α, *i*) is calculated as follows:

$$BD_{\mathrm{GNSRPP}}(N,\alpha,i)=2\cdot\left|\frac{\alpha}{\pi}+\frac{2}{N}\cdot(i-1)-1\right|-1. \quad (11)$$

C. Flag of Single-Phase ESC Occurrence

Naturally sampled modulation is taken as an example to analyze. For the previous carrier pattern *Pattern*(*N*, α, *i*) and the current carrier pattern *Pattern*(*N*, α, *j*), the flag of the single-phase ESC occurrence at time *t* is expressed as

$$\begin{aligned}&\mathrm{Flag}\,(N,\mathrm{ph},t,\alpha,i,j)\\&=\begin{pmatrix}\mathrm{sign}\,(BD(N,\alpha,i)-VR_{\mathrm{ph}}\,(t))\\ \times\mathrm{sign}\,(VR_{\mathrm{ph}}\,(t)-BD(N,\alpha,j))\\ +\mathrm{sign}\,(VR_{\mathrm{ph}}\,(t)-BD(N,\alpha,i))\\ \times\mathrm{sign}\,(BD(N,\alpha,j)-VR_{\mathrm{ph}}\,(t))\end{pmatrix}\end{aligned} \quad (12)$$

where ph = *A*, *B*, and *C* for three phases, $BD(N,\alpha,i)$ can be either $BD_{\mathrm{GNSRPP}}(N,\alpha,i)$ for GNSRPP-SVPWM(*N*, α) or $BD_{\mathrm{NSRPP}}(N,0,i)$ for NSRPP-SVPWM, and the function "sign()" is defined as

$$\mathrm{sign}\,(x)=\begin{cases}1, x\geq 0\\ 0, x<0\end{cases}. \quad (13)$$

The understanding of (12) is that single-phase ESCs include the following two cases at the boundaries of the carrier periods.

1) *From "low level" to "high level":* "sign($BD(N,\alpha,i)-VR_{\mathrm{ph}}(t)$)" is the result of comparing the boundary value of *Pattern*(*N*, α, *i*) with the reference wave value at time *t*. When the comparison result is 1, the output phase leg voltage is low level at the end of the previous carrier period. When the comparison result is 0, the output phase leg voltage is high level at the end of the previous carrier period. Therefore, when the product of "sign($BD(N,\alpha,i)-VR_{\mathrm{ph}}(t)$)" and "sign($VR_{\mathrm{ph}}(t)-BD(N,\alpha,j)$)" is 1, the output phase leg voltage is low level at the end of the previous carrier period and high level at the beginning of the current carrier period, as shown in Fig. 6(a). A single-phase ESC from low level to high level occurs at the beginning of the current carrier period.
2) *From "high level" to "low level":* Similarly, when the product of "sign($VR_{\mathrm{ph}}(t)-BD(N,\alpha,i)$)" and "sign($BD(N,\alpha,j)$ - $VR_{\mathrm{ph}}(t)$)" is 1, the output phase leg voltage is high level at the end of the previous carrier period and low level at the beginning of the current carrier period. A single-phase ESC from high level to low level occurs at the beginning of the current carrier period.

D. Calculation Results

For NSRPP-SVPWM and the proposed GNSRPP-SVPWM, all *N* fundamental carrier patterns can be selected. Therefore, all cases where the previous carrier pattern and the current carrier pattern are any two of the *N* fundamental carrier patterns should be considered.

The occurrence probabilities of single-phase ESC, simultaneous two-phase switching operation, and simultaneous three-phase switching operation are calculated as (14), (15) shown at the bottom of this next page, and (16), respectively

$$\begin{aligned}&P1\,(N,\alpha)\\&=\frac{1}{N^2}\sum_{i=1}^{N}\sum_{j=1}^{N}\left[\frac{1}{2\pi}\cdot\int_0^{2\pi}\mathrm{Flag}\,(N,\mathrm{ph},t,\alpha,i,j)\,d\,(\omega_0 t)\right]\end{aligned} \quad (14)$$

$$\begin{aligned}&P3\,(N,\alpha)=\frac{1}{N^2}\sum_{i=1}^{N}\\&\sum_{j=1}^{N}\left[\frac{1}{2\pi}\cdot\int_0^{2\pi}\begin{pmatrix}\mathrm{Flag}\,(N,A,t,\alpha,i,j)\\ \times\mathrm{Flag}\,(N,B,t,\alpha,i,j)\\ \times\mathrm{Flag}\,(N,C,t,\alpha,i,j)\end{pmatrix}d\,(\omega_0 t)\right].\end{aligned} \quad (16)$$

For several α angles, the calculation results of the ESC occurrence probabilities of G4SRPP-SVPWM and G6SRPP-SVPWM are shown in Figs. 7 and 8, where OP_ESC1, OP_S2, and OP_S3 are the occurrence probabilities of single-phase ESC, simultaneous two-phase switching operation, and simultaneous three-phase switching operation, respectively. The following can be clearly seen.

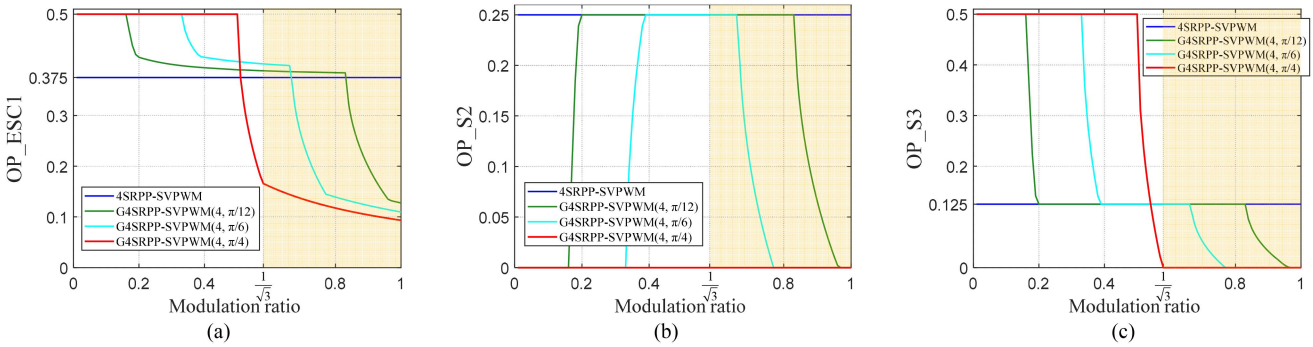

Fig. 7. Calculation results of occurrence probabilities of ESCs for 4SRPP-SVPWM and several G4SRPP-SVPWM strategies. (a) OP_ESC1. (b) OP_S2. (c) OP_S3.

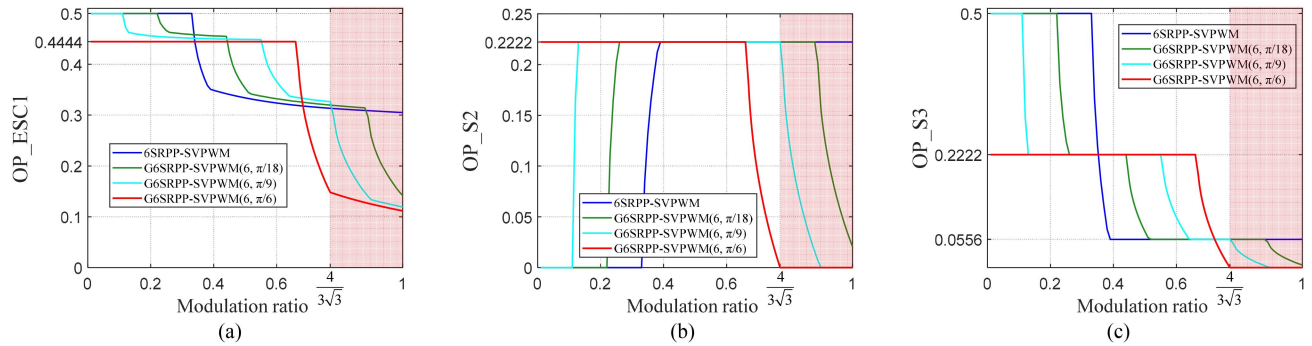

Fig. 8. Calculation results of occurrence probabilities of ESCs for 6SRPP-SVPWM and several G6SRPP-SVPWM strategies. (a) OP_ESC1. (b) OP_S2. (c) OP_S3.

1) As shown in Fig. 7, for the proposed G4SRPP-SVPWM(4, $\pi/4$), during the modulation ratio range of $a \geq \frac{1}{\sqrt{3}}$, simultaneous two- or three-phase switching operations are completely avoided, and single-phase ESCs are significantly reduced.
2) As shown in Fig. 8, for the proposed G6SRPP-SVPWM(6, $\pi/6$), during the modulation ratio range of $a \geq \frac{4}{3\sqrt{3}}$, simultaneous two- or three-phase switching operations are completely avoided, and single-phase ESCs are significantly reduced.

E. Recommended GNSRPP-SVPWM Strategies to Avoid or Reduce ESCs

Obviously, there are many design options for GNSRPP-SVPWM (N, α). A group of design recommendations are given as follows.

1) G2SRPP-SVPWM (2, $\pi/2$) is recommended to be used in full modulation ratio range to significantly disperse the odd-order PWM harmonics without any ESC occurrence.
2) GNSRPP-SVPWM (N, π/N) with even number N ($N \geq 4$) is recommended to be used in the modulation ratio range

$$P2\left(N,\alpha\right)=\frac{1}{N^2}\sum_{i=1}^{N}\sum_{j=1}^{N}\left[\frac{1}{2\pi}\cdot\int_0^{2\pi}\left(\begin{array}{l}\left(\begin{array}{l}\text{Flag}\left(N,A,t,\alpha,i,j\right)\\ \times\text{Flag}\left(N,B,t,\alpha,i,j\right)\\ \times\left(1-\text{Flag}\left(N,C,t,\alpha,i,j\right)\right)\end{array}\right)\\ +\left(\begin{array}{l}\text{Flag}\left(N,A,t,\alpha,i,j\right)\\ \times\left(1-\text{Flag}\left(N,B,t,\alpha,i,j\right)\right)\\ \times\text{Flag}\left(N,C,t,\alpha,i,j\right)\end{array}\right)\\ +\left(\begin{array}{l}\left(1-\text{Flag}\left(N,A,t,\alpha,i,j\right)\right)\\ \times\text{Flag}\left(N,B,t,\alpha,i,j\right)\\ \times\text{Flag}\left(N,C,t,\alpha,i,j\right)\end{array}\right)\end{array}\right)d\left(\omega_0 t\right)\right] \tag{15}$$

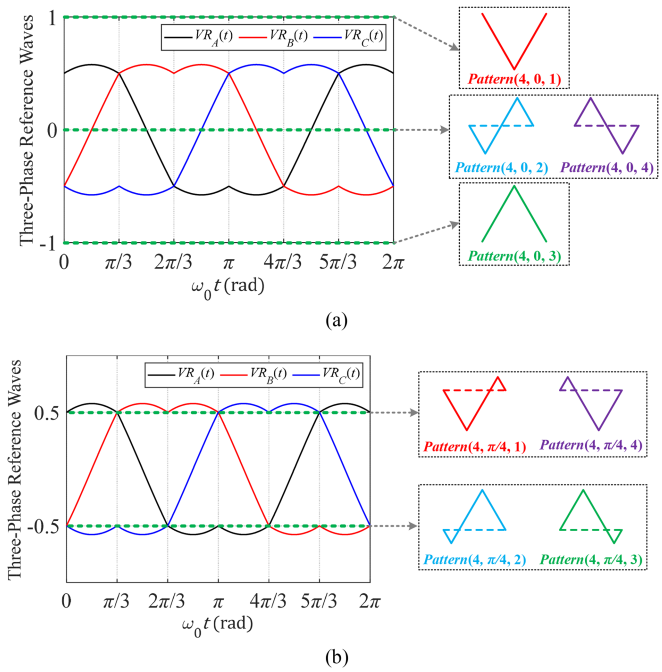

Fig. 9. Three-phase reference waves with $a = \frac{1}{\sqrt{3}}$ and the boundaries of the four fundamental carrier patterns. (a) 4SRPP-SVPWM. (b) G4SRPP-SVPWM $(4, \pi/4)$.

of $a \geq \frac{2}{\sqrt{3}} \times (2 \cdot |\frac{\pi/N}{\pi} - 1| - 1)$ to significantly reduce single-phase ESCs, and completely avoid simultaneous two- or three-phase switching operations. Besides, it can significantly disperse all PWM harmonics except those located nearby the *N*th carrier frequency and its multiples.

Specifically, 2SRPP-SVPWM randomly selects the inverted and noninverted triangular carrier patterns with the boundary values of "1" and "−1" for each carrier period. Since three-phase reference values are always between "1" and "−1," simultaneous three-phase switching operation will occur when the carrier pattern is switched to the other one. In contrast, for the proposed G2SRPP-SVPWM$(2, \pi/2)$, its two fundamental carrier patterns with the phases of 90° and 270° have the equal boundary value "0," which completely avoids ESCs.

For the proposed GNSRPP-SVPWM$(N, \pi/N)$ strategies with even number N $(N \geq 4)$, when the modulation ratio satisfies $a \geq \frac{2}{\sqrt{3}} \times (2 \cdot |\frac{\pi/N}{\pi} - 1| - 1)$, there are always two phases whose reference wave values are always larger or smaller than the boundary values of all fundamental carrier patterns, thereby avoiding simultaneous two- or three-phase switching operations. And single-phase ESC is only possible to occur in the phase with the medium duty cycle.

Taking $N = 4$ as an example to analyze, Fig. 9 shows the three-phase reference waves (the modulation ratio $a = 1/\sqrt{3}$) and the boundary values of the four fundamental carrier patterns when using 4SRPP-SVPWM and G4SRPP-SVPWM$(4, \pi/4)$, respectively. For 4SRPP-SVPWM, the boundary values of the four fundamental carrier patterns are "1, 0, −1, and 0." Therefore, as shown in Fig. 9(a), when switching between different carrier patterns, ESC may occur at the boundaries of the carrier periods. In contrast, for the proposed G4SRPP-SVPWM$(4, \pi/4)$, the boundary values of the four fundamental carrier patterns are "0.5, −0.5,−0.5 and 0.5," as shown in Fig. 9(b). Under the premise of $a \geq \frac{1}{\sqrt{3}}$, there are always two phases whose reference wave values are always larger or smaller than "0.5 and −0.5." Therefore, simultaneous two- or three-phase switching operation can be completely avoided, and only the phase with the medium duty cycle may introduce single-phase ESC.

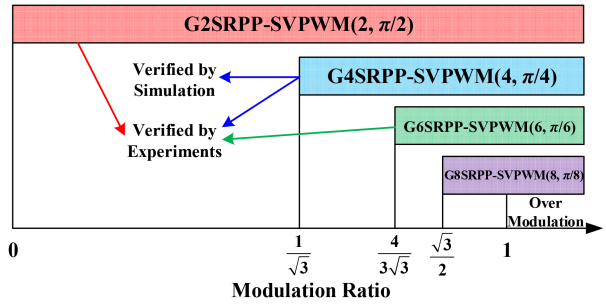

Fig. 10. Applicable modulation ratio ranges to avoid or reduce ESCs for some recommended GNSRPP-SVPWM strategies.

Above all, the applicable modulation ratio ranges to avoid or reduce ESCs for some recommended GNSRPP-SVPWM strategies are shown in Fig. 10. Specifically, G2SRPP-SVPWM$(2, \pi/2)$ is applicable to avoid ESCs in full modulation range, G4SRPP-SVPWM$(4, \pi/4)$ is applicable to avoid or reduce ESCs with $a \geq \frac{1}{\sqrt{3}}$, G6SRPP-SVPWM$(6, \pi/6)$ is applicable to avoid or reduce ESCs with $a \geq \frac{4}{3\sqrt{3}}$, and G8SRPP-SVPWM$(8, \pi/8)$ is applicable to avoid or reduce ESCs with $a \geq \frac{\sqrt{3}}{2}$. For other modulation strategies with larger *N* values, the applicable modulation ratio ranges to avoid or reduce ESCs can be calculated. The larger the value of *N*, the smaller the applicable modulation ratio range that can avoid or reduce ESCs.

IV. Switching Power Loss Analysis of the Proposed GNSRPP-SVPWM Strategies

Compared with the conventional SVPWM, the proposed GNSRPP-SVPWM does not change three-phase duty cycles. Therefore, conduction power losses remain unchanged, and analysis of switching power losses is the focus of this section.

According to [34], switching losses essentially vary proportionally to the magnitude of the instantaneous load current, for an inverter operating with a constant dc bus voltage. Hence, the switching power losses of the conventional SVPWM for a switching phase leg over one half of a fundamental period are approximately

$$P_{\text{loss(con)}} = V_e I_m \frac{1}{\pi} \int_{-\frac{\pi}{2}}^{\frac{\pi}{2}} |\cos(\theta - \varphi)| \, d\theta \tag{17}$$

where V_e is an equivalent dc voltage for determining the switching losses, and φ is the power factor angle.

For NSRPP-SVPWM, the ESC may occur in all three phases. Hence, the switching power losses of NSRPP-SVPWM for a

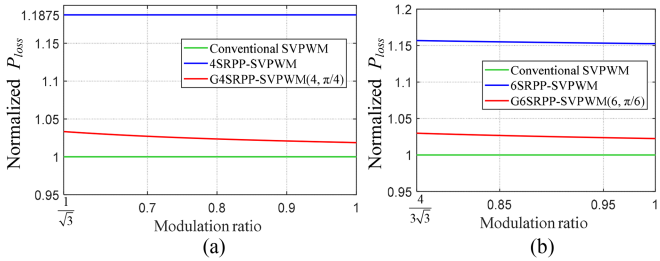

Fig. 11. Comparison of normalized switching power losses of conventional SVPWM, NSRPP-SVPWM, and GNSRPP-SVPWM (N, π/N) with the unity power factor and different modulation ratios. (a) $N = 4$. (b) $N = 6$.

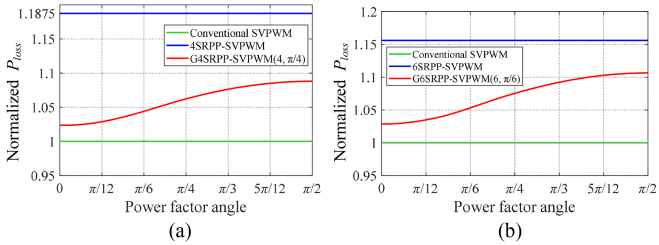

Fig. 12. Comparison of normalized switching power losses of conventional SVPWM, NSRPP-SVPWM, and GNSRPP-SVPWM(N, π/N) with different power factor angles and the modulation ratio $a = 0.8$. (a) $N = 4$. (b) $N = 6$.

switching phase leg are approximately

$$P_{\text{loss(NSRPP)}} = (1 + 0.5 \cdot P1_{\text{NSRPP}}) \cdot V_e I_m \frac{1}{\pi} \int_{-\frac{\pi}{2}}^{\frac{\pi}{2}} |\cos(\theta - \varphi)| \, d\theta \quad (18)$$

where $P1_{\text{NSRPP}}$ is the occurrence probability of a single-phase ESC for NSRPP-SVPWM.

For the proposed GNSRPP-SVPWM, the ESC is only possible to occur in the phase with the medium duty cycle so that

$$P_{\text{loss(GNSRPP)}} = V_e I_m \frac{1}{\pi} \int_{-\frac{\pi}{2}}^{\frac{\pi}{2}} |\cos(\theta - \varphi)| \, d\theta + \frac{1}{2} P1_{\text{GNSRPP}} \cdot V_e I_m \frac{1}{\pi} \times \begin{pmatrix} \int_{-\frac{\pi}{2}}^{-\frac{\pi}{3}} |\cos(\theta - \varphi)| \, d\theta + \int_{-\frac{\pi}{3}}^{0} \left|\cos\left(\theta - \varphi + \frac{2}{3}\pi\right)\right| d\theta \\ + \int_{0}^{\frac{\pi}{3}} \left|\cos\left(\theta - \varphi - \frac{2}{3}\pi\right)\right| d\theta + \int_{\frac{\pi}{3}}^{\frac{\pi}{2}} |\cos(\theta - \varphi)| \, d\theta \end{pmatrix} \quad (19)$$

where $P1_{\text{GNSRPP}}$ is the occurrence probability of the single-phase ESC for GNSRPP-SVPWM.

Taking the switching power loss of the conventional SVPWM as the base value, the normalized switching power losses of 4SRPP-SVPWM, 6SRPP-SVPWM, G4SRPP-SVPWM(4, $\pi/4$), and G6SRPP-SVPWM(6, $\pi/6$) are shown in Figs. 11 and 12. For convenience, the power factor in Fig. 11 is fixed at 1, and the modulation ratio in Fig. 12 is fixed at 0.8. From Fig. 12, it can be clearly seen that in high power factor applications, the switching power loss of the proposed GNSRPP-SVPWM is much smaller than that of NSRPP-SVPWM. However, when

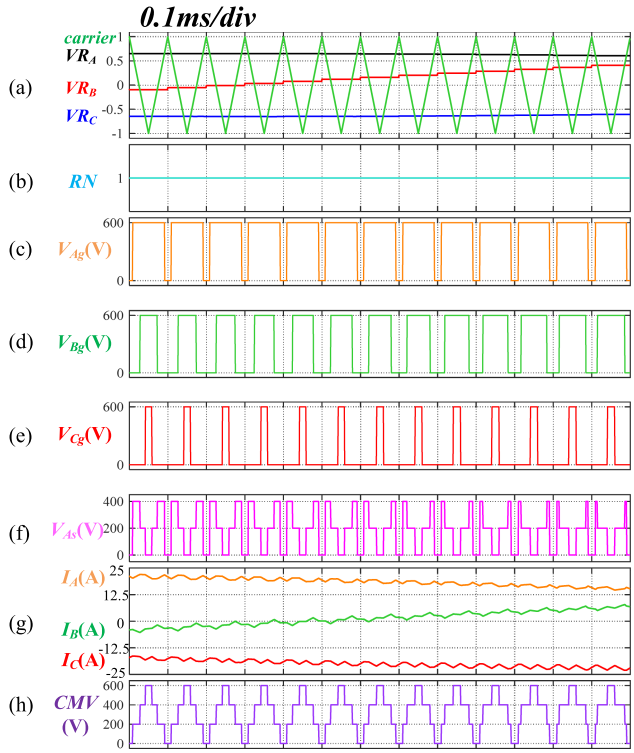

Fig. 13. Key time-domain waveforms of conventional SVPWM at the modulation ratio $a = 0.65$. (a) Three-phase reference waves and the carrier wave. (b) Random number *RN*. (c) *A*-phase-leg voltage. (d) *B*-phase-leg voltage. (e) *C*-phase-leg voltage. (f) *A*-phase voltage. (g) Three-phase currents. (h) CMV.

$N \geq 4$, the switching power loss of the proposed GNSRPP-SVPWM(N, π/N) is slightly larger than that of the conventional SVPWM, which is the shortcoming of the proposed strategy. When designing an inverter, the switching power loss should be evaluated based on the analysis in this section to achieve a tradeoff between the inverter efficiency and PWM harmonic dispersion performance.

V. Simulations and Discussion

In this section, G4SRPP-SVPWM(4, $\pi/4$) will be verified to maintain constant carrier frequency, achieve excellent PWM harmonics dispersion performance, and avoid or reduce ESCs at the same time.

A three-phase two-level VSI model using regularly sampled modulation is built in MATLAB/Simulink. Relevant simulations are conducted with $V_{\text{dc}} = 600$ V, the carrier frequency $f_c = 10$ kHz, the fundamental frequency $f_0 = 60$ Hz, the *RL* load $R = 10\Omega$, $L = 2$ mH, and the power factor angle $\varphi = 4.31°$. Besides, the modulation ratio a is set to 0.65, which is slightly larger than $\frac{1}{\sqrt{3}}$.

A. Time-Domain Waveforms: Observe Avoidance or Reduction of ESCs

Sector I is taken as an example to observe. For conventional SVPWM, 4SRPP-SVPWM, and the proposed G4SRPP-SVPWM(4, $\pi/4$), Figs. 13–15 show their key time-domain

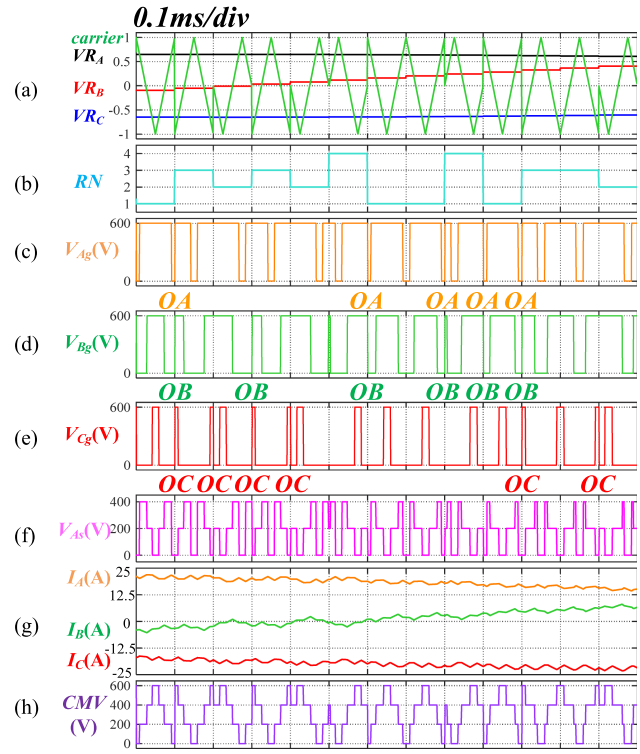

Fig. 14. Key time-domain waveforms of 4SRPP-SVPWM at the modulation ratio $a = 0.65$. (a) Three-phase reference waves and the carrier wave. (b) Random number *RN*. (c) *A*-phase-leg voltage. (d) *B*-phase-leg voltage. (e) *C*-phase-leg voltage. (f) *A*-phase voltage. (g) Three-phase currents. (h) CMV.

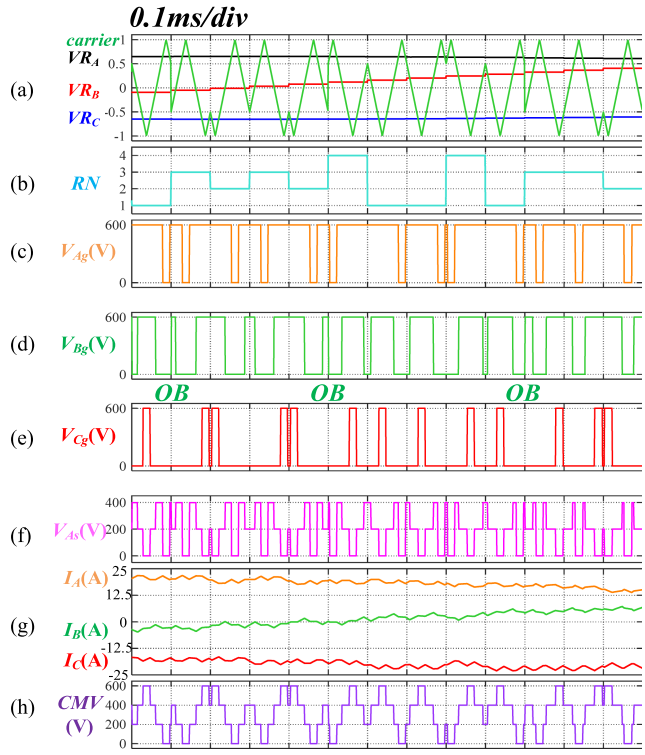

Fig. 15. Key time-domain waveforms of G4SRPP-SVPWM (4, $\pi/4$) at the modulation ratio $a = 0.65$. (a) Three-phase reference waves and the carrier wave. (b) Random number *RN*. (c) *A*-phase-leg voltage. (d) *B*-phase-leg voltage. (e) *C*-phase-leg voltage. (f) *A*-phase voltage. (g) Three-phase currents. (h) CMV.

waveforms of three-phase reference waves (VR_A, VR_B, and VR_C) and the carrier wave, random number *RN*, three-phase leg voltages (V_{Ag}, V_{Bg}, and V_{Cg}), *A*-phase voltage V_{As}, three-phase currents, and CMV. From the time-domain waveforms of three-phase leg voltages (V_{Ag}, V_{Bg}, and V_{Cg}), ESCs can be clearly observed by the operations of three-phase switches (**OA**, **OB,** and **OC**) at the boundaries of carrier periods.

As shown in Fig. 13, key waveforms of the conventional SVPWM are roughly periodic, which will make some components dominant in the frequency domain.

As shown in Fig. 14, for 4SRPP-SVPWM, simultaneous two- or three-phase switching operations will occur at the boundaries of the carrier periods when switching between different fundamental carrier patterns. And the random selection of the four fundamental carrier patterns disrupts the approximate periodicity of the key waveforms.

As shown in Fig. 15, for the proposed G4SRPP-SVPWM(4, $\pi/4$), simultaneous two- or three-phase switching operations are completely avoided, and single-phase ESCs are significantly reduced. ESCs are only possible to occur in phase *B* with the medium duty cycle. Besides, the random selection of the four fundamental carrier patterns still disrupts the approximate periodicity of the key waveforms.

B. Spectrum Analysis: Observe PWM Harmonics Dispersion

To verify the PWM harmonics dispersion performance, Fig. 16 shows the spectrum analysis of phase current (relative to fundamental) and CMV (relative to V_{dc}) for different modulation strategies.

From Fig. 16(a), it can be clearly seen that when using the conventional SVPWM, dominant PWM harmonics will appear around the carrier frequency and its integer multiples, which is the inherent limitation of the conventional SVPWM. The proposed strategy is an effective and costless method to solve this problem. It can be clearly seen from Fig. 16(b) and (c) that both 4SRPP-SVPWM and G4SRPP-SVPWM(4, $\pi/4$) can significantly disperse the $(4k+1)$th, $(4k+2)$th, and $(4k+3)$th PWM harmonics in both DM and CM domains, while the $(4k+4)$th PWM harmonics remain unchanged.

C. Comparison With Traditional RPWM Strategies

Fig. 17 shows the spectrum analysis of phase current (relative to fundamental) and CMV (relative to V_{dc}) for several traditional RPWM strategies.

For RCF-SVPWM strategies with the carrier period range (95 μs, 105 μs) and the carrier period range (80 μs, 120 μs), Fig. 17(a) and (b) shows their spectrum analysis of phase current and CMV. It can be seen that wider carrier period range disperses PWM harmonics more effectively. Besides, the proposed G4SRPP-SVPWM(4, $\pi/4$) disperses the PWM harmonics more effectively than RCF-PWM at the carrier frequency and its double multiple.

Fig. 17(c) and (d) shows the spectrum analysis of RCD-PWM and RZD-PWM strategies. It can be clearly seen that their PWM harmonics dispersion performance is far inferior to the proposed G4SRPP-SVPWM(4, $\pi/4$).

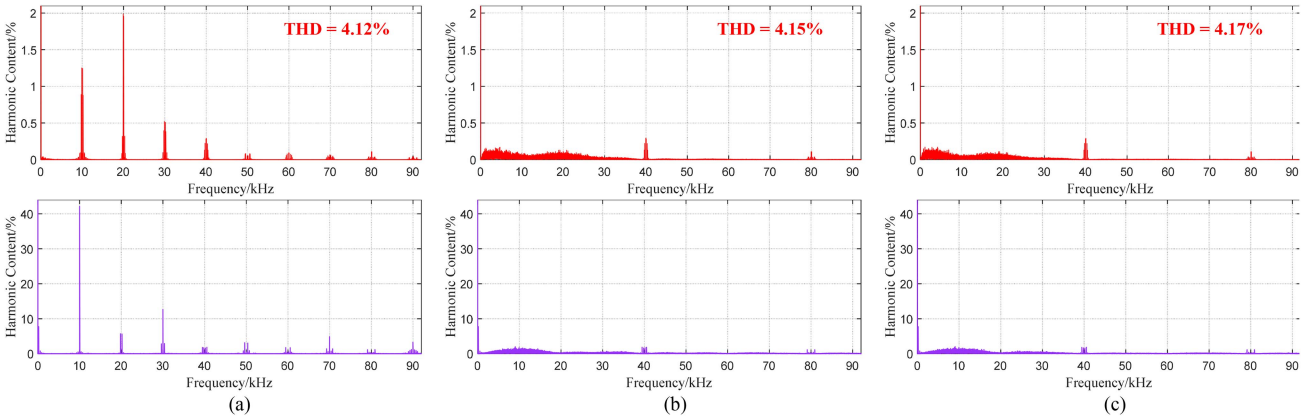

Fig. 16. Spectrum analysis of (top) phase current (relative to fundamental) and (bottom) CMV (relative to V_{dc}) with the modulation ratio a = 0.65. (a) Conventional SVPWM. (b) 4SRPP-SVPWM. (c) G4SRPP-SVPWM (4, $\pi/4$).

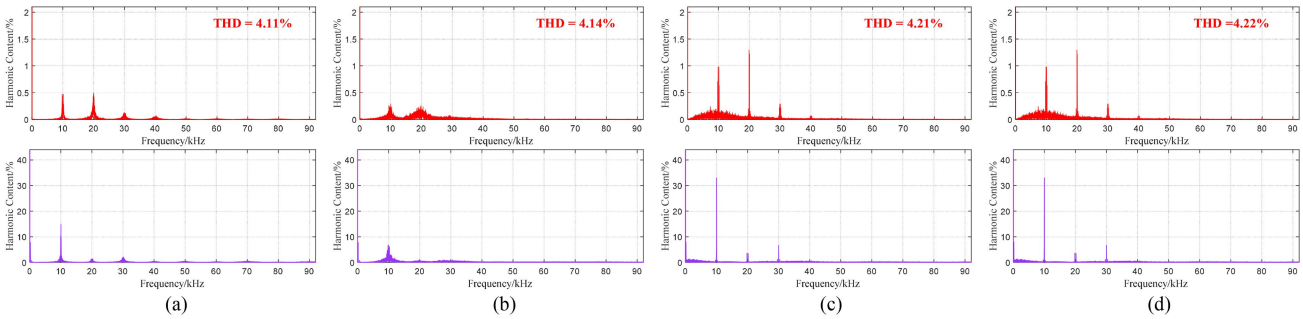

Fig. 17. Spectrum analysis of (top) phase current (relative to fundamental) and (bottom) CMV (relative to V_{dc}) for the traditional RPWM strategies with the modulation ratio $a = 0.65$. (a) RCF-SVPWM, carrier period range (95 μs, 105 μs). (b) RCF-SVPWM, carrier period range (80 μs, 120 μs). (c) RCD-PWM. (d) RZD-PWM.

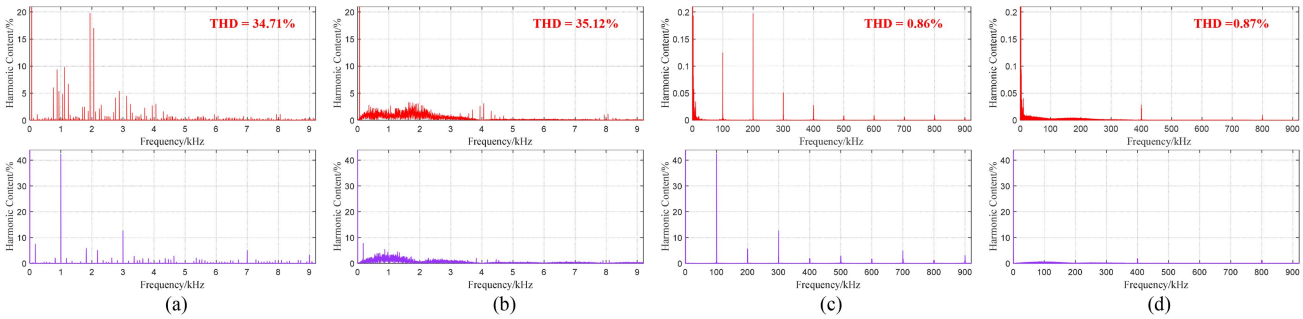

Fig. 18. Spectrum analysis of (top) phase current (relative to fundamental) and (bottom) CMV (relative to V_{dc}) with the modulation ratio $a = 0.65$ and different carrier frequencies. (a) Conventional SVPWM with the carrier frequency $f_c = 1$ kHz. (b) G4SRPP-SVPWM (4, $\pi/4$) with the carrier frequency $f_c = 1$ kHz. (c) Conventional SVPWM with the carrier frequency $f_c = 100$ kHz. (d) G4SRPP-SVPWM (4, $\pi/4$) with the carrier frequency $f_c = 100$ kHz.

Fig. 18(a) and (b) shows the spectrum analysis for the conventional SVPWM and the proposed G4SRPP-SVPWM(4, $\pi/4$) when the carrier frequency is 1 kHz. Fig. 18(c) and (d) shows the spectrum analysis when the carrier frequency is 100 kHz. It can be seen that the proposed G4SRPP-SVPWM(4, $\pi/4$) can still significantly disperse the $(4k + 1)$th, $(4k + 2)$th, and $(4k + 3)$th PWM harmonics in both DM and CM domains. The proposed strategy is effective in both low- and high-switching-frequency applications.

From the total harmonic distortion (THD) results marked in the upper right corner of Figs. 16–18, one can see that the RPWM strategies cannot reduce the current THD, which is the inherent limitation of the RPWM technology.

D. Comparison of Switching Power Loss

For convenience, turn-ON switching energy and turn-OFF switching energy are considered to be proportional to the magnitude of the instantaneous load current.

Instantaneous currents at switching instants are obtained through MATLAB/Simulink. By changing the resistance and inductance without changing their impedance magnitude, the

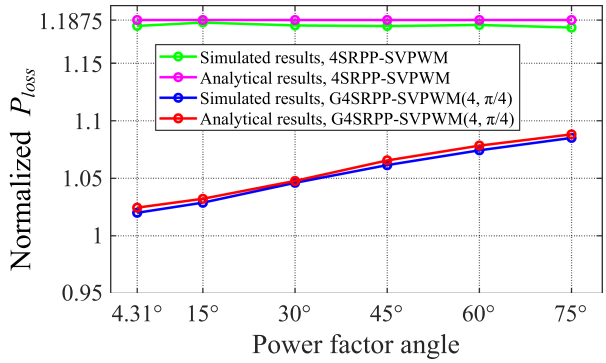

Fig. 19. Comparison of simulated and theoretical normalized switching power losses when $N = 4$.

TABLE I
TEST IPMSM PARAMETERS

Parameters	Value
Stator resistance	$R_s = 0.55\ \Omega$
Direct axis inductance	$L_d = 6.5$ mH
Quadrature axis inductance	$L_q = 20.6$ mH
Permanent magnet flux linkage	$\Psi_f = 0.18$ Wb
Pole-pairs	3
Motor speed	$n = 2500$ r/min
Load torque	$T_L = 8.35$ N·m

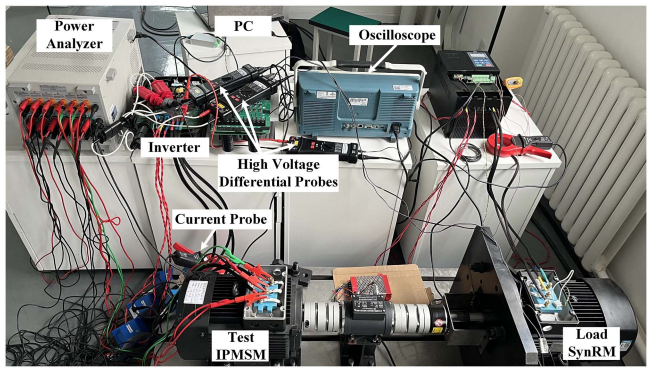

Fig. 20. Photograph of experimental platform.

simulation results of the normalized switching power losses with different power factors at the same current magnitude can be obtained. The comparison of simulated and theoretical normalized switching power losses is shown in Fig. 19, from which it can be seen that they are basically consistent. In high power factor applications, although the switching power loss of the proposed G4SRPP-SVPWM(4, $\pi/4$) is slightly larger than that of the conventional SVPWM, it is much smaller than that of 4SRPP-SVPWM.

VI. EXPERIMENTAL RESULTS AND ANALYSIS

To verify the effectiveness of the proposed GNSRPP-SVPWM, an IPMSM sensorless drive system has been built. And the IPMSM system parameters are given in Table I. The photograph of the experimental platform is shown in Fig. 20.

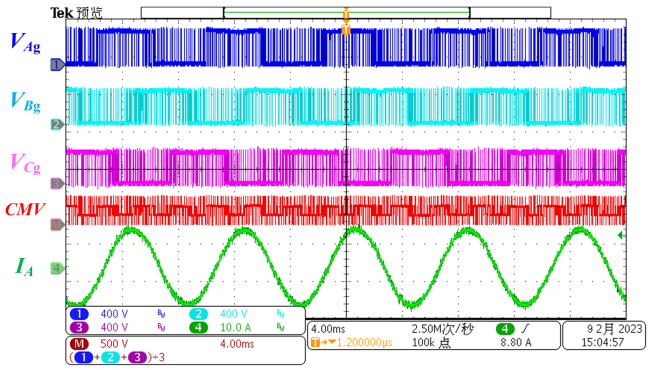

Fig. 21. Experimental time-domain waveforms for spectrum analysis.

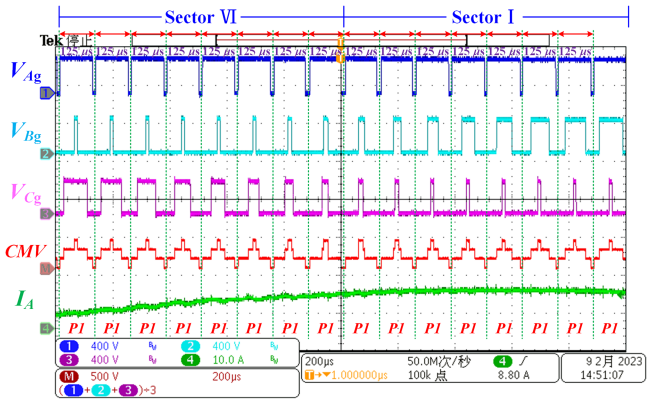

Fig. 22. Zoom of the time-domain waveforms for conventional SVPWM in Sectors VI and I.

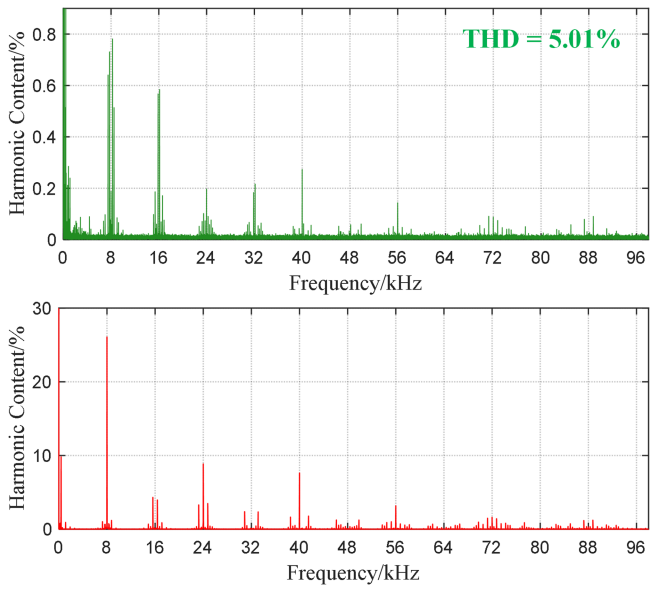

Fig. 23. Spectrum analysis of (top) phase current (relative to fundamental) and (bottom) CMV (relative to V_{dc}) for the conventional SVPWM.

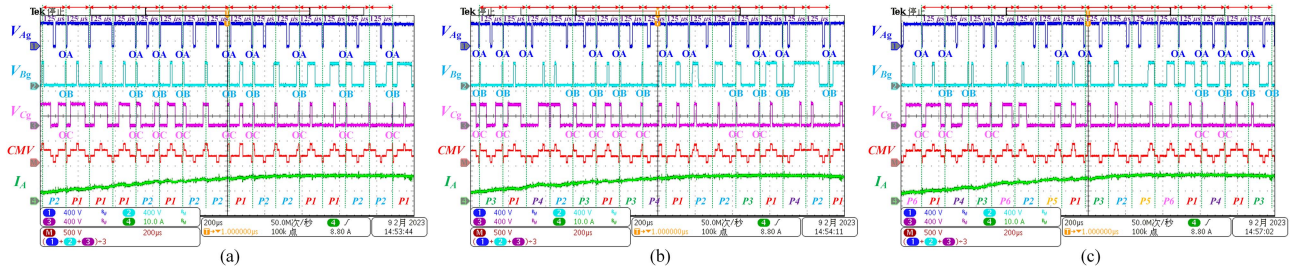

Fig. 24. Zooms of time-domain waveforms for NSRPP-SVPWM strategies in Sectors VI and I. (a) 2SRPP-SVPWM. (b) 4SRPP-SVPWM. (c) 6SRPP-SVPWM.

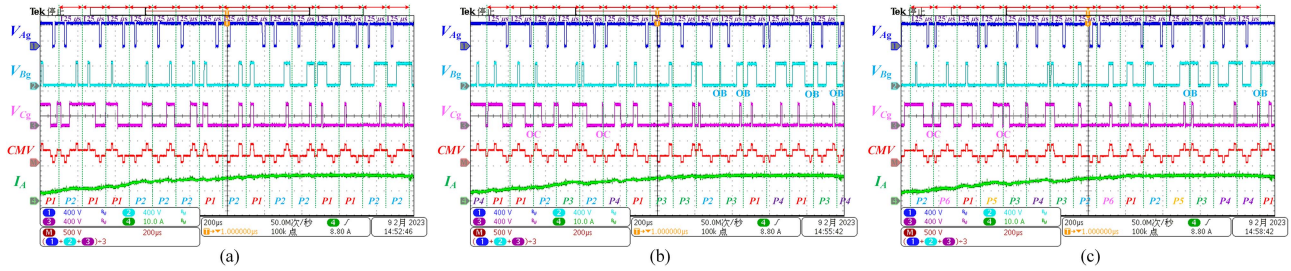

Fig. 25. Zooms of time-domain waveforms for the proposed GNSRPP-SVPWM strategies in Sectors VI and I. (a) G2SRPP-SVPWM (2, $\pi/2$). (b) G4SRPP-SVPWM (4, $\pi/4$). (c) G6SRPP-SVPWM (6, $\pi/6$).

The phase voltage and phase current are measured by high-voltage differential probe and currents probes, respectively. The dc-link voltage $V_{\rm dc}$ is set to 360 V. The carrier frequency $f_{\rm c}$ is set to 8 kHz. And the motor is set to operate at 2500 r/min with 8.35-N·m load torque. At this working condition, the modulation ratio $a \approx 0.81$, which is larger than both $\frac{1}{\sqrt{3}}$ and $\frac{4}{3\sqrt{3}}$.

The time-domain waveforms used for spectrum analysis are shown in Fig. 21, which shows the three-phase leg voltages, CMV, and the *A*-phase current sequentially from top to bottom.

For the conventional SVPWM, zoom of the time-domain waveform is shown in Fig. 22, where the first half and the second half of the waveform correspond to Sectors VI and I, respectively. The spectrum analysis of phase current (relative to fundamental) and CMV (relative to $V_{\rm dc}$) is shown in Fig. 23. It can be clearly seen that the PWM harmonics located nearby the carrier frequency and its integer multiples are dominant, which is the inherent limitation of the conventional SVPWM.

RPWM strategies aim to disperse the dominant PWM harmonics, and their discussions are as follows.

A. Avoidance or Reduction of ESCs

For NSRPP-SVPWM and GNSRPP-SVPWM(N, π/N) with $N = 2$, 4, and 6, zooms of experimental time-domain waveforms in Sectors VI and I are shown in Figs. 24 and 25. The *i*th fundamental carrier pattern is abbreviated as "*Pi*." ESCs can be clearly observed by the operations of three-phase switches (**OA**, **OB,** and **OC**) at the boundaries of carrier periods.

As shown in Fig. 24, it can be clearly seen that for NSRPP-SVPWM strategies with $N = 2$, 4, and 6, lots of ESCs "**OA**, **OB,** and **OC**" occur at the boundaries of the carrier periods, including simultaneous two- or three-phase switching operations.

In contrast, as shown in Fig. 25(a), no ESC occurs when using G2SRPP-SVPWM(2, $\pi/2$). Besides, for G4SRPP-SVPWM(4, $\pi/4$) and G6SRPP-SVPWM(6, $\pi/6$) as shown in Fig. 25(b) and (c), simultaneous two- or three-phase switching operations are completely avoided, and single-phase ESC is only possible to occur in the phase with the medium duty cycle.

B. Effectiveness of PWM Harmonics Dispersion

To verify the PWM harmonics dispersion performance, Figs. 26 and 27 show the spectrum analysis of phase current (relative to fundamental) and CMV (relative to $V_{\rm dc}$) for NSRPP-SVPWM and the proposed GNSRPP-SVPWM strategies.

The proposed GNSRPP-SVPWM strategies have basically the same PWM harmonics dispersion performance as NSRPP-SVPWM strategies. Specifically, Figs. 26(a) and 27(a) verify that both 2SRPP-SVPWM and G2SRPP-SVPWM(2, $\pi/2$) significantly disperse the odd-order PWM harmonics in both DM and CM domains. Figs. 26(b) and 27(b) verify that both 4SRPP-SVPWM and G4SRPP-SVPWM(4, $\pi/4$) significantly disperse the $(4k+1)$th, $(4k+2)$th, and $(4k+3)$th PWM harmonics in both DM and CM domains, while the $(4k+4)$th PWM harmonics remain unchanged. And Figs. 26(c) and 27(c) verify that both 6SRPP-SVPWM and G6SRPP-SVPWM(6, $\pi/6$) can significantly disperse the $(6k+1)$th, $(6k+2)$th, $(6k+3)$th, $(6k+4)$th, and $(6k+5)$th PWM harmonics in both DM and CM domains, while the $(6k+6)$th PWM harmonics remain unchanged.

It is worth noting that the phase currents' THDs of conventional SVPWM, NSRPP-SVPWM, and the proposed GNSRPP-SVPWM strategies are similar.

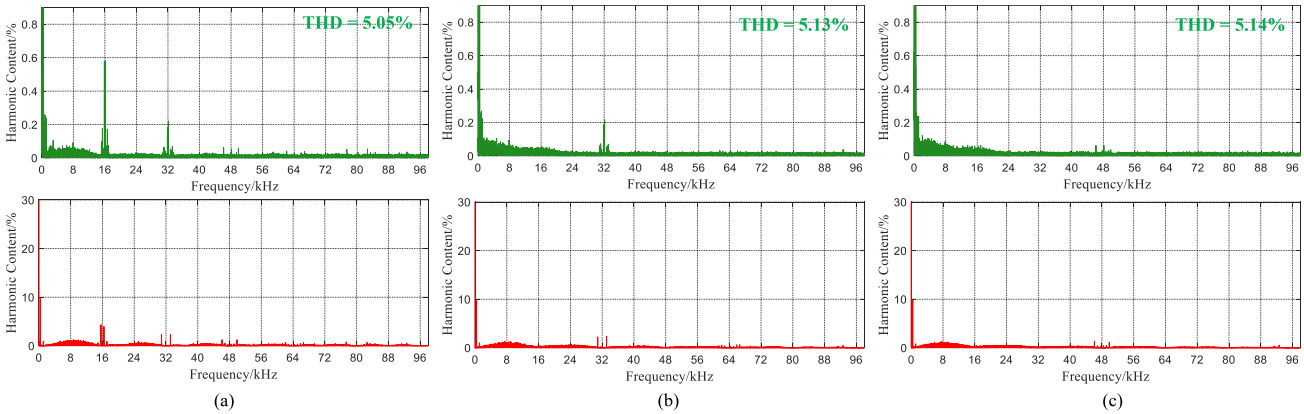

Fig. 26. Spectrum analysis of (top) phase current (relative to fundamental) and (bottom) CMV (relative to $V_{\rm dc}$) for NSRPP-SVPWM strategies. (a) 2SRPP-SVPWM. (b) 4SRPP-SVPWM. (c) 6SRPP-SVPWM.

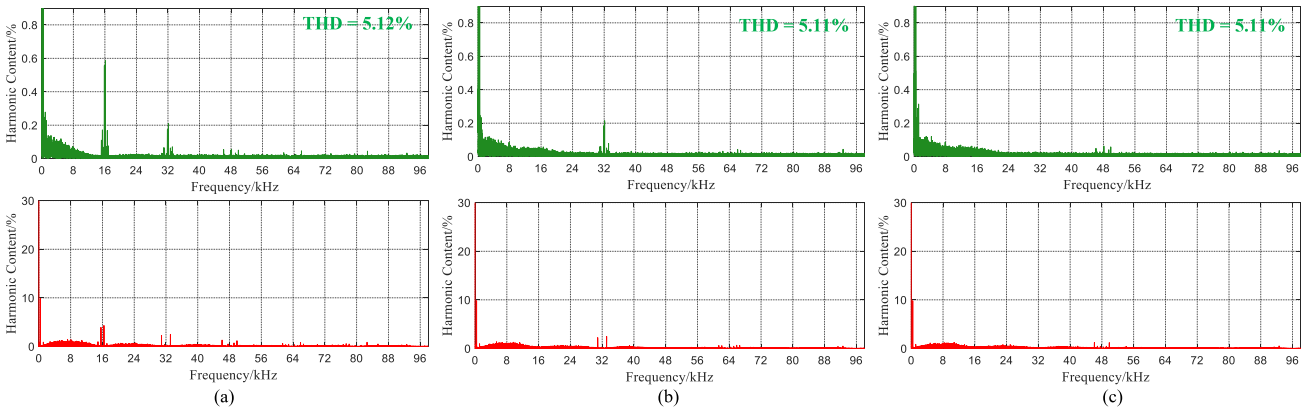

Fig. 27. Spectrum analysis of (top) phase current (relative to fundamental) and (bottom) CMV (relative to $V_{\rm dc}$) for the proposed GNSRPP-SVPWM strategies. (a) G2SRPP-SVPWM(2, π/2). (b) G4SRPP-SVPWM(4, π/4). (c) G6SRPP-SVPWM(6, π/6).

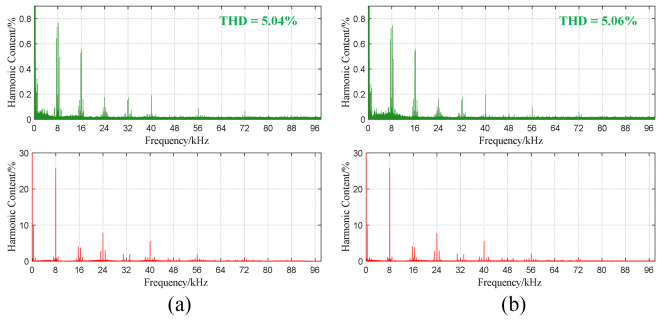

Fig. 28. Spectrum analysis of (top) phase current (relative to fundamental) and (bottom) CMV (relative to $V_{\rm dc}$) for (a) RCD-PWM and (b) RZD-PWM.

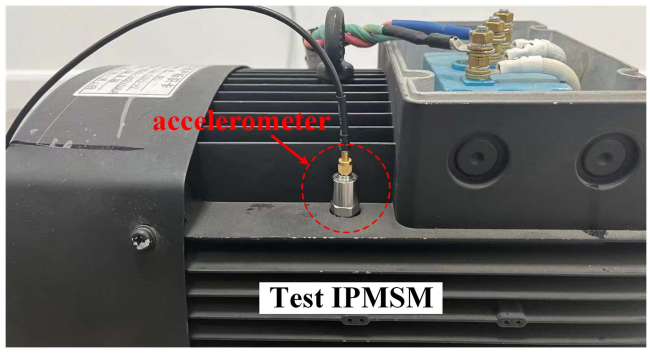

Fig. 29. Position of the accelerometer.

C. Comparison With Traditional RPWM Strategies

For comparison, Fig. 28 shows the spectrum analysis of FCF-RPWM strategies without ESCs. It can be clearly seen that the PWM harmonics dispersion performance of RCD-PWM and RZD-PWM is far inferior to the proposed GNSRPP-SPWM.

In addition, RCF-PWM cannot start the motor smoothly even in the narrow carrier period range (124 μs, 126 μs) corresponding to the carrier frequency range (7.937 kHz, 8.065 kHz) due to the variation of sampling frequency, which affects the controller parameters and sensorless control algorithm.

D. Inverter Power Loss and Inverter Efficiency

For aforementioned modulation strategies, their experimental results of inverter power losses and inverter efficiency are

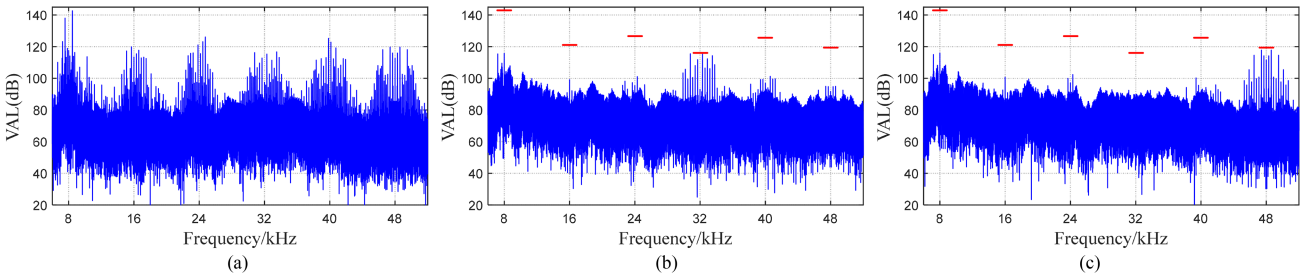

Fig. 30. Spectrum analysis of the vibration acceleration of the stator surface. (a) Conventional SVPWM. (b) G4SRPP-SVPWM(4, $\pi/4$). (c) G6SRPP-SVPWM(6, $\pi/6$).

TABLE II
EXPERIMENTAL RESULTS OF INVERTER POWER LOSSES AND INVERTER EFFICIENCY

Modulation strategies	Inverter power losses	Inverter efficiency
Conventional SVPWM	87.44 W	96.40 %
RCD-PWM	87.41 W	96.42 %
RZD-PWM	87.49 W	96.39 %
2SRPP-SVPWM	94.98 W	96.10 %
4SRPP-SVPWM	93.12 W	96.17 %
6SRPP-SVPWM	92.13 W	96.21 %
G2SRPP-SVPWM(2, π/2)	87.51 W	96.41 %
G4SRPP-SVPWM(4, π/4)	88.59 W	96.37 %
G6SRPP-SVPWM(6, π/6)	88.35 W	96.38 %

shown in Table II, from which it can be clearly seen that RCD-PWM, RZD-PWM, and G2SRPP-SVPWM(2, $\pi/2$) do not introduce extra inverter power losses. When $N = 4$ and 6, although the inverter power loss of the proposed GNSRPP-SVPWM is slightly larger than that of the conventional SVPWM, it is much smaller than that of NSRPP-SVPWM. Correspondingly, when $N = 4$ and 6, although the inverter efficiency of the proposed GNSRPP-SVPWM is lower than that of conventional SVPWM, it is higher than that of NSRPP-SVPWM.

E. Surface Vibration of the Stator

One of the applications of the proposed GNSRPP-SVPWM is the reduction of the dominant high-frequency vibration harmonics. As shown in Fig. 29, the vibration acceleration of the stator surface is measured by an accelerometer. For the conventional SVPWM and proposed GNSRPP-SVPWM, the comparison of the vibration acceleration level (VAL) of the test IPMSM is shown in Fig. 30, and the VAL can be expressed as

$$L_a = 20\log_{10}\frac{A}{A_o} \tag{20}$$

where $A_o = 1 \times 10^{-6}$ m/s^2 is the reference acceleration and A is the measured acceleration. The VAL L_a can be described in decibels (dB).

It can be clearly seen that when using the conventional SVPWM as shown in Fig. 30(a), dominant high-frequency vibration harmonics will appear around the carrier frequency and its integer multiples. When using the proposed G4SRPP-SVPWM (4, $\pi/4$) as shown in Fig. 30(b), only the high-frequency vibration harmonics around 32 kHz remain unchanged, while the other high-frequency vibration harmonics are significantly dispersed. And when using the proposed G6SRPP-SVPWM (6, $\pi/6$) as shown in Fig. 30(c), only the high-frequency vibration harmonics around 48 kHz remain unchanged, while the other high-frequency vibration harmonics are significantly dispersed. This is consistent with the mathematical analysis. Therefore, it can be seen that the proposed GNSRPP-SVPWM is an effective method to suppress high-frequency vibrations caused by PWM technology.

VII. CONCLUSION

The proposed GNSRPP-SVPWM is an effective and costless method to significantly disperse the dominant PWM harmonics over a wider frequency band, thereby suppressing the discrete peak harmonics. The recommended GNSRPP-SVPWM strategies aim to further overcome the shortcomings of NSRPP-SVPWM leading to ESCs.

The comparison of different modulation strategies is given in Table III. Compared with the conventional SVPWM, the proposed GNSRPP-SVPWM can significantly disperse the dominant PWM harmonics at the expense of slightly increased switching power loss. Through mathematical analysis, simulations, and experimental validation, the advantages of the recommended GNSRPP-SVPWM strategies over other RPWM strategies can be summarized as follows.

1) Constant sampling frequency: The proposed GNSRPP-SVPWM maintains the constant carrier frequency and the constant sampling frequency, thereby achieving applicability in sensorless closed-loop vector control of the IPMSM.
2) Excellent PWM harmonics dispersion performance: The proposed GNSRPP-SVPWM can significantly disperse all PWM harmonics except those located nearby the *N*th carrier frequency and its multiples.
3) Avoidance or reduction of ESCs: The recommended G2SRPP-SVPWM(2, $\pi/2$) does not introduce any ESC. And the recommended GNSRPP-SVPWM(N, π/N) with even number N ($N \geq 4$) completely avoids simultaneous two- or three-phase switching operations, and only the phase with the medium duty cycle may introduce single-phase ESC.

TABLE III
COMPARISON OF DIFFERENT MODULATION STRATEGIES

	Conventional SVPWM	RCF-PWM	RCD-PWM and RZD-PWM	NSRPP-SVPWM	GNSRPP-SVPWM(N, π/N) with even number N
Harmonics dispersion performance	Worst	Average	Bad	Good	Good
Current sampling frequency	Constant	Variable	Constant	Constant	Constant
Closed-loop system	Applicable	Not applicable	Applicable	Applicable	Applicable
Applicable modulation ratio range	Full range	Full range	Low range	Full range	$a \geq \frac{2}{\sqrt{3}} \times \left(2 \cdot \left\lvert \frac{\pi/N}{\pi} - 1 \right\rvert - 1\right)$
Simultaneous multiphase switching	No	No	No	Yes	No
Switching power loss	Comparison base value	Similar	Similar	Significantly increased	Similar or slightly increased

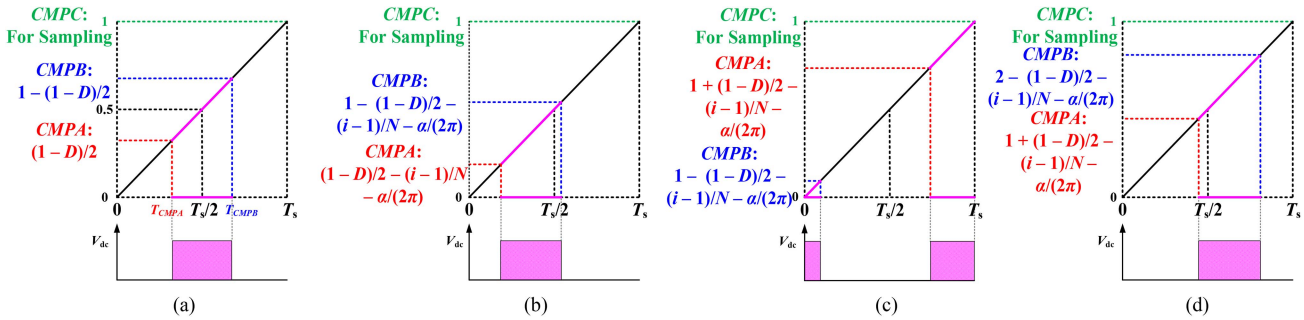

Fig. 31. Illustration of DSP implementation with up-count mode. (a) Conventional SVPWM. Three cases of the proposed GNSRPP-SVPWM: (b) case 1, (c) case 2, and (d) case 3.

APPENDIX

In the experiments of this article, TMS320F280025 DSP chip with 100-MHz clock frequency is used to drive the inverter switches of a three-phase two-level VSI. Since the essence of the carrier phase shift is to move the output pulse, three counter-compare values can realize any form of carrier phase shift, i.e., counter-compare A register (CMPA) is used to trigger the high output voltage, counter-compare B register (CMPB) is used to trigger the low output voltage, and counter-compare 0 (CMP0) is used to change the polarity of the output phase leg voltage at the beginning of the carrier period.

Taking up-count mode as an example to analyze, a straight line is used to represent the stair step of counting, and expressions with duty cycle D are used to represent the counter-compare value. The calculations of CMPA and CMPB for conventional SVPWM are shown in Fig. 31(a).

For the proposed GNSRPP-SVPWM, since the ith carrier pattern has the carrier phase-shift angle of $(\alpha + (i-1) \times \frac{2\pi}{N})$, there are the following three cases for the DSP implementation of the (i)th carrier pattern.

1) *Case 1:* As shown in Fig. 31(b), "CMPA ≥ 0" and "CMPB ≥ 0" still hold after CMPA and CMPB are subtracted by the same value corresponding to the carrier pattern. At this time, CMP0 is used to trigger the low output voltage.
2) *Case 2:* As shown in Fig. 31(c), it satisfies that "CMPA < 0" and "CMPB ≥ 0" after CMPA and CMPB are subtracted by the same value corresponding to the carrier pattern. At this time, add 1 to CMPA and set CMP0 to trigger the high output voltage.
3) *Case 3:* As shown in Fig. 31(d), it satisfies that "CMPA < 0" and "CMPB < 0" after CMPA and CMPB are subtracted by the same value corresponding to the carrier pattern. At this time, add 1 to both CMPA and CMPB, and set CMP0 to trigger the low output voltage.

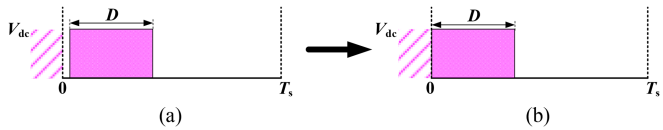

Fig. 32. Operations of extremely narrow low-level pulse at the beginning of the carrier period. (a) Before termination. (b) After termination.

Counter-compare C register (CMPC) is used to trigger analog-to-digital converter (ADC) sampling. In this article, CMPC is set to "$D = 1$," i.e., ADC sampling is triggered at the end of the previous carrier period, which can avoid the noise caused by the possible switching operation at the beginning of the current carrier period.

In the experiments of this article, pulses with pulsewidth within $T_N = 1.25$ μs are considered to be extremely narrow pulses and are terminated. Termination of extremely narrow low-level pulse at the beginning of the carrier period is taken as an example to show in Fig. 32. As shown in Fig. 32(a), without terminating the extremely narrow low-level pulse, the phase leg voltage outputs high level at the end of the previous carrier period, switches to low level at the beginning of the current carrier period, and then, switches to high level within 1.25 μs again. The extremely narrow low-level pulse can be terminated without changing the duty cycle by shifting the entire high-level pulse as shown in Fig. 32(b). Other termination operations can be performed in the same way.

REFERENCES

[1] Y. Shen, Q. Wang, D. Liu, Y. Wang, Z. Zheng, and H. Li, "A mixed SVPWM technique for three-phase current reconstruction with single DC negative rail current sensor," *IEEE Trans. Power Electron.*, vol. 37, no. 5, pp. 5357–5372, May 2022.

[2] Y.-S. Lai, Y.-K. Lin, and C.-W. Chen, "New hybrid pulsewidth modulation technique to reduce current distortion and extend current reconstruction range for a three-phase inverter using only DC-link sensor," *IEEE Trans. Power Electron.*, vol. 28, no. 3, pp. 1331–1337, Mar. 2013.
[3] Y. Huang, Y. Xu, W. Zhang, and J. Zou, "Hybrid RPWM technique based on modified SVPWM to reduce the PWM acoustic noise," *IEEE Trans. Power Electron.*, vol. 34, no. 6, pp. 5667–5674, Jun. 2019.
[4] Y. Lv et al., "Spatial-harmonic modeling and analysis of high-frequency electromagnetic vibrations of multiphase surface permanent-magnet motors," *IEEE Trans. Ind. Electron.*, vol. 70, no. 12, pp. 11865–11875, Dec. 2023.
[5] K. Hatua, A. K. Jain, D. Banerjee, and V. T. Ranganathan, "Active damping of output LC filter resonance for vector-controlled VSI-fed AC motor drives," *IEEE Trans. Ind. Electron.*, vol. 59, no. 1, pp. 334–342, Jan. 2012.
[6] Y. Huang, Y. Xu, W. Zhang, and J. Zou, "PWM frequency noise cancellation in two-segment three-phase motor using parallel interleaved inverters," *IEEE Trans. Power Electron.*, vol. 34, no. 3, pp. 2515–2525, Mar. 2019.
[7] X. Zhu et al., "A passive variable switching frequency SPWM concept and analysis for DCAC converter," *IEEE Trans. Power Electron.*, vol. 37, no. 5, pp. 5524–5534, May 2022.
[8] A. Peyghambari, A. Dastfan, and A. Ahmadyfard, "Selective voltage noise cancellation in three-phase inverter using random SVPWM," *IEEE Trans. Power Electron.*, vol. 31, no. 6, pp. 4604–4610, Jun. 2016.
[9] H. Li, Z. Yang, B. Wang, V. G. Agelidis, and B. Zhang, "On thermal impact of chaotic frequency modulation SPWM techniques," *IEEE Trans. Ind. Electron.*, vol. 64, no. 3, pp. 2032–2043, Mar. 2017.
[10] A. Dove, J. Naudé, and I. Hofsajer, "An argument for the relationship between spectral spreading and probability spreading for EMI-reduction in DC–DC converter," *IEEE Trans. Power Electron.*, vol. 35, no. 2, pp. 1459–1472, Feb. 2020.
[11] F. Bu, T. Pu, W. Huang, and L. Zhu, "Performance and evaluation of five-phase dual random SVPWM strategy with optimized probability density function," *IEEE Trans. Ind. Electron.*, vol. 66, no. 5, pp. 3323–3332, May 2019.
[12] J. Xu, Z. Nie, and J. Zhu, "Characterization and selection of probability statistical parameters in random slope PWM based on uniform distribution," *IEEE Trans. Power Electron.*, vol. 36, no. 1, pp. 1184–1192, Jan. 2021.
[13] Y. Wu, J. Xu, T. B. Soeiro, M. Stecca, and P. Bauer, "Optimal periodic variable switching PWM for harmonic performance enhancement in grid-connected voltage source converters," *IEEE Trans. Power Electron.*, vol. 37, no. 6, pp. 7247–7262, Jun. 2022.
[14] J. Huang and K. Li, "Suppressing the maximum EMI spectral peak through asynchronous carriers in the three-phase inverter with the periodic CFM," *IEEE Trans. Power Electron.*, vol. 37, no. 4, pp. 3702–3707, Apr. 2022.
[15] Z. Ji, S. Cheng, Q. Ren, X. Li, Y. Lv, and D. Wang, "The effects and mechanisms of periodic-carrier-frequency PWM on vibrations of multiphase permanent magnet synchronous motors," *IEEE Trans. Power Electron.*, vol. 38, no. 7, pp. 8696–8706, Jul. 2023.
[16] Z. Ji, S. Cheng, Y. Lv, D. Wang, W. Sun, and X. Li, "The mechanism for suppressing high-frequency vibration of multiphase surface permanent magnet motors via PWM carrier phase shifting," *IEEE Trans. Power Electron.*, vol. 36, no. 9, pp. 10504–10513, Sep. 2021.
[17] L. Mathe, F. Lungeanu, D. Sera, P. O. Rasmussen, and J. K. Pedersen, "Spread spectrum modulation by using asymmetric-carrier random PWM," *IEEE Trans. Ind. Electron.*, vol. 59, no. 10, pp. 3710–3718, Oct. 2012.
[18] R. L. Kirlin, C. Lascu, and A. M. Trzynadlowski, "Shaping the noise spectrum in power electronic converters," *IEEE Trans. Ind. Electron.*, vol. 58, no. 7, pp. 2780–2788, Jul. 2011.
[19] Y.-S. Lai, Y.-T. Chang, and B.-Y. Chen, "Novel random-switching PWM technique with constant sampling frequency and constant inductor average current for digitally controlled converter," *IEEE Trans. Ind. Electron.*, vol. 60, no. 8, pp. 3126–3135, Aug. 2013.
[20] A. M. Trzynadlowski, K. Borisov, Y. Li, and L. Qin, "A novel random PWM technique with low computational overhead and constant sampling frequency for high-volume, low-cost applications," *IEEE Trans. Power Electron.*, vol. 20, no. 1, pp. 116–122, Jan. 2005.
[21] F. Bu et al., "Analysis and performance of five-phase piecewise-random-switching-frequency space vector pulse width modulation," *IEEE Trans. Energy Convers.*, vol. 36, no. 3, pp. 2339–2347, Sep. 2021.
[22] Z. Ji, S. Cheng, X. Li, Y. Lv, and D. Wang, "An optimal periodic carrier frequency PWM scheme for suppressing high-frequency vibrations of permanent magnet synchronous motors," *IEEE Trans. Power Electron.*, vol. 38, no. 10, pp. 13008–13018, Oct. 2023.
[23] M. M. Bech, F. Blaabjerg, and J. K. Pedersen, "Random modulation techniques with fixed switching frequency for three-phase power converters,"
[24] Y.-C. Lim, S.-O. Wi, J.-N. Kim, and Y.-G. Jung, "A pseudorandom carrier modulation scheme," *IEEE Trans. Power Electron.*, vol. 25, no. 4, pp. 797–805, Apr. 2010.
[25] K.-S. Kim, Y.-G. Jung, and Y.-C. Lim, "A new hybrid random PWM scheme," *IEEE Trans. Power Electron.*, vol. 24, no. 1, pp. 192–200, Jan. 2009.
[26] Y.-S. Lai and B.-Y. Chen, "New random PWM technique for a full-bridge DC/DC converter with harmonics intensity reduction and considering efficiency," *IEEE Trans. Power Electron.*, vol. 28, no. 11, pp. 5013–5023, Nov. 2013.
[27] R. Wang, Z. Lin, J. Du, J. Wu, and X. He, "Direct sequence spread spectrum-based PWM strategy for harmonic reduction and communication," *IEEE Trans. Power Electron.*, vol. 32, no. 6, pp. 4455–4465, Jun. 2017.
[28] P. Zhang, S. Wang, and Y. Li, "Performance and analysis of N-state random pulse position SVPWM with constant sampling frequency," *IEEE Trans. Power Electron.*, vol. 37, no. 11, pp. 13606–13625, Nov. 2022.
[29] A. M. Hava and E. Ün, "A high-performance PWM algorithm for common-mode voltage reduction in three-phase voltage source inverters," *IEEE Trans. Power Electron.*, vol. 26, no. 7, pp. 1998–2008, Jul. 2011.
[30] A. M. Hava and E. Ün, "Performance analysis of reduced common-mode voltage PWM methods and comparison with standard PWM methods for three-phase voltage-source inverters," *IEEE Trans. Power Electron.*, vol. 24, no. 1, pp. 241–252, Jan. 2009.
[31] E. Un and A. M. Hava, "On the contribution of PWM methods to the common mode (leakage) current in conventional three-phase two-level inverters as applied to AC motor drives," in *Proc. IEEE Ind. Appl. Soc. Annu. Meeting*, 2008, pp. 1–8.
[32] J. Xu, J. Han, Y. Wang, M. Ali, and H. Tang, "High-frequency SiC three-phase VSIs with common-mode voltage reduction and improved performance using novel tri-state PWM method," *IEEE Trans. Power Electron.*, vol. 34, no. 2, pp. 1809–1822, Feb. 2019.
[33] D. Grahame Holmes and T. A. Lipo, "Modulation of three-phase voltage source inverters," in *Pulse Width Modulation for Power Converters: Principles and Practice*. New York, NY, USA: Wiley, 2003, pp. 215–258.
[34] D. Grahame Holmes and T. A. Lipo, "Zero space vector placement modulation strategies," in *Pulse Width Modulation for Power Converters: Principles and Practice*. New York, NY, USA: Wiley, 2003, pp. 259–336.

Peiran Zhang received the B.S. degree in electrical engineering from Shandong University, Jinan, China, in 2020. He is currently working toward the Ph.D. degree in electrical engineering with Tsinghua University, Beijing, China.

His research interests include power converter, motor drive, and sensorless control.

Shanming Wang (Senior Member, IEEE) received the B.S. and M.S. degrees in electrical engineering from Nanchang University, Nanchang, China, in 1993 and 1996, respectively, and the Ph.D. degree in electrical engineering from Tsinghua University, Beijing, China, in 2001.

In 2001, he joined the Department of Electrical Engineering, Tsinghua University, where he is currently a Professor. His research interests include the analysis and control of electric machines, vibration analysis of electrical machines, hybrid excitation permanent-magnet machines, the simulation of ac machines and systems, and fault analysis for electric machines and its protection.

Yituo Li received the Ph.D. degree in electrical engineering from Tsinghua University, Beijing, China, in 2013.

He is currently a research staff with Tsinghua University. His main interests include high-performance ac drives and sensorless control.